

Shear-horizontal surface acoustic wave sensor for non-invasive monitoring of dynamic cell spreading and attachment in wound healing assays

Manuel S. Brugger, Lukas G. Schnitzler, Timo Nieberle, Achim Wixforth, Christoph Westerhausen

Angaben zur Veröffentlichung / Publication details:

Brugger, Manuel S., Lukas G. Schnitzler, Timo Nieberle, Achim Wixforth, and Christoph Westerhausen. 2021. "Shear-horizontal surface acoustic wave sensor for non-invasive monitoring of dynamic cell spreading and attachment in wound healing assays." *Biosensors and Bioelectronics* 173: 112807.
<https://doi.org/10.1016/j.bios.2020.112807>.

Shear-Horizontal Surface Acoustic Wave Sensor for Non-Invasive Monitoring of Dynamic Cell Spreading and Attachment in Wound Healing Assays

Manuel S. Brugger^{1,2}, Lukas G. Schnitzler^{1,3}, Timo Nieberle¹, Achim Wixforth^{1,3,4}, Christoph Westerhausen^{1,3,4,5}

¹Experimental Physics I, Institute of Physics, Experimental Physics I, University of Augsburg, 86159 Augsburg, Germany

²Stiftung der Deutschen Wirtschaft (sdw) gGmbH, Breite Straße 29, 10178 Berlin, Germany

³Center for NanoScience (CeNS), Ludwig-Maximilians-Universität Munich, 80799 Munich, Germany

⁴Augsburg Center for Innovative Technologies (ACIT), 86159 Augsburg, Germany

⁵Physiology, Institute of Theoretical Medicine, University of Augsburg, 86159 Augsburg, Germany

Corresponding Author:

Christoph Westerhausen

University of Augsburg, Chair of Experimental Physics I, Universitätstr. 1, 86159 Augsburg

Tel.: +049-821-598 3311

christoph.westerhausen@gmail.com

M.S.B., A.W. and C.W. designed the study; M.S.B., T.N. performed experiments, M.S.B. analyzed data; L.G.S. performed the simulations; and M.S.B., L.G.S., A. W., T. N. and C.W. wrote the manuscript.

ABSTRACT

A Love-wave based biosensor is introduced for analyzing a standardized wound healing assay by observing cell growth and quantifying cell detachment processes. Utilizing the piezoelectric material LiTaO₃ 36° XY-cut with a thin SiO₂-cover layer, shear horizontal surface acoustic waves (SAW) are excited and detected by a set of Interdigital Transducers. Epithelial cells, being cultivated on the substrate and invading the sensors delay line are causing a phase shift in the transmitted SAW signal. This phase shift correlates exactly with the surface coverage of the invading cells. After wound healing, emerging fluctuations in the phase shift signal provide information about the cell growth in a confluent cell layer. Additionally, the signal slope allows to quantify the cell detachment process induced by apoptosis, necrosis or cell lysis substances, respectively. Furthermore, culture conditions like temperature or osmolality can be simultaneously monitored by SAW. Based on a theoretical approach and using FEM simulations, we identified the acoustoelectric interaction as the main reason for the phase shift in various frequency- and time dependent studies. Our model is validated by experimental data and allows predicting the phase change caused by variations in the cell-substrate distance or the volume ratio of the nucleus to the complete cell.

Keywords: Love-Wave, Wound-Healing-Assay, cell adhesion, bio-chip, detachment, FEM

INTRODUCTION

Cell adhesion and migration play a crucial role in multicellular organisms. Cells are in contact with each other and with an extracellular matrix (ECM). Studying cell adhesion and cell substrate interaction is therefore fundamental for biotechnologies like cell culture, tissue engineering, drug discovery and biomaterials. Especially for implant research, the biocompatibility and cell adhesion strength is of highest interest^{1,2}.

Monitoring the cell activity by, e.g., reporter gene expression, fluorescent target translocation or second messenger generation require methods that often are prone to compromising the cell physiology³. Therefore, label-free, non-invasive sensing methods offer an advantageous approach allowing for a real-time monitoring of cellular processes without interference. Among these, one can distinguish the following types: electric, optical and acoustic sensors³⁻⁷. Particularly piezoelectric techniques employing acoustic sensors fulfil the demands and offer a unique possibility to study cellular mechanisms without interference as they are *inter alia* sensitive to mass coupling, viscoelastic or electric properties changes close to the sensor surface^{3,7}. So far, the underlying principles of acoustic sensors can be categorized into two groups: Those using bulk acoustic waves (e.g. quartz crystal microbalance (QCM) resonators) and those using surface acoustic waves (SAW). The important parameter is the working frequency and the possibility of spatial resolution. The higher the frequency, the better the sensors sensitivity⁸. QCM for instance, can detect mass deposition and viscoelastic changes in the adjacent medium through changes in the resonance frequency and a certain insertion loss. Due to this effect, studies for cell attachment and spreading mechanisms are implemented which demonstrate a linear relationship between surface cell coverage and changes in resonance frequency of the quartz crystal⁹⁻¹⁴. As the working frequency is dependent on the membrane thickness, the typical frequency range of QCM-sensors is 10-50 MHz. At higher frequencies, the membrane thickness would become too fragile for a practical use. In contrast, SAW devices are not bound by these restrictions. First reported in the 1990s^{15,16}, these SAW sensors are especially sensitive to property changes on the surface due to the high resonance frequency in the MHz-GHz range. They have become increasingly used for *in situ* probing of mass loading and evaluation of material properties of biological layers. For biological sensing applications, which typically are done in a liquid environment, SAW sensors usually use pseudo shear-horizontal surface acoustic waves (SH-SAW) with no

vertical deflection of the surface. In contrast, Rayleigh Waves have successfully been shown to positively interact with cells to stimulate migration^{17,18}, proliferation¹⁹ and at much higher amplitudes also uptake^{20,21}. These surface confined acoustic, mechanical waves are coupling to any medium being in contact with the surface. The SAW phase velocity and amplitude is hereby strongly affected by the presence of layers being deposited on the sensing surface. The measured amplitude and phase information of a transmission signal, denoted as S_{21} , can then be used to investigate the properties of the material on the surface³. Employing this technology, different studies have been performed: protein adsorption and interaction, lipid research or polymer analysis²². SH-sensors have been successfully employed in the last ten years especially in the field of cell sedimentation, adhesion and spreading^{23,24}, cell-substrate interaction²⁵ or as a cell-based biosensor for toxin detection²⁶. Furthermore, first investigations were performed detecting the cellular damage due to hydrogen peroxide treatment²⁷.

However, none of the studies mentioned have so far investigated the dynamic process of already adhered cells moving on a free surface and healing an artificial wound. A related approach to measure wound healing employs electrochemical impedance spectroscopy [5]. However, this approach comes along with invasive wound creation and limitations regarding spatial resolution.

Here, we present and characterize a method to monitor the healing of an artificial wound by employing a SH-SAW device in a simple delay-line geometry in order to access the migration rate of cells. Additionally, changes in a confluent cell layer and cell detachment processes were measured and quantified. Additional finite elements simulations support the experimental findings.

MATERIALS AND METHODS

SAW-chip

SAW are generated on a small piezoelectric chip where micron sized metal electrodes, so-called Interdigital Transducers (IDT) are supplied with an rf signal. This rf signal is then effectively converted into a well-defined, piezoacoustic surface wave. The SAW exited on the chosen material lithium tantalate in 36° rot YX-cut (LiTaO_3) has a negligible component normal to the surface and therefore is operated in a quasi-shear-horizontal mode²⁸. This shear wave excites no energy dissipating compression waves in liquid environments and has therefore been used in various sensing applications e.g. for biosensors²⁹.

IDTs are deposited on top of the substrate by using standard lithography techniques. They consist of two

multi-finger interdigitated electrodes (Ti-Au-Ti, $d_{Ti} = 5$ nm, $d_{Au} = 50$ nm) and are adjusted to the radio frequency (rf)-systems impedance of $Z = 50$ Ohm, as first described by White and Voltmer³⁰. The comb-like structures used in our experiments have 33 finger pairs with a length of 500 μ m (aperture). The width between two fingers of the same polarity was chosen to be $d = 20$ μ m and defines the wavelength $\lambda = d$ of the generated SAW. Due to the propagation velocity of the chosen lithium tantalate cut $v_{36^\circ \text{rot-YX-lithium tantalate}} = 4150$ m/s, the theoretical resonance frequency f_{res} of the IDTs is $f_{res} = 207$ MHz for a free surface. The distance between the emitting IDT-1 and the receiving IDT-2 is $l = 500$ μ m (delay-line). The total sensitive area (IDT-1, IDT-2 and delay-line) covers a chip area of 0,91 mm² of which 0,25 mm² belong to the delay-line (Fig. 1 A-2)).

In order to avoid corrosion of the metallic structures, to ensure biocompatibility and to obtain a high sensitivity to surface effects, a $t = 150$ nm thick SiO₂ layer was deposited by thermal evaporation on the whole SAW-chip except for the contact pads. The SiO₂ layer additionally serves as an acoustic waveguide layer by confining the SAW on the surface resulting in a Love-wave³¹. For simplification, the wave is called 'SAW' in the following. The surface acoustic wave sensors parameters are the amplitude and the phase of the wave, which are related to acoustic velocity and intensity, respectively, and are being measured as a function of time.

The SAW – measurand interaction is only sensitive within a certain distance to the surface, as the displacement of the liquid induced by coupling to the SAW is confined to this layer. The thickness of this layer is called penetration depth δ and can be calculated by $\delta = \sqrt{2\eta/\omega\rho_f}$ ⁷ for viscous fluids.

For our parameters and pure water on the surface we obtain $\delta = 40$ nm, but according to Saitakis et al.³² a higher penetration depth of around $\delta = 100$ nm can be safely assumed since the presence of cells leads to a higher viscosity close to the surface.

Cells and culturing

In this study, we use the epithelial cell line 'Madine-Darby Canine Kidney' (MDCK-II) (ECACC Cat.No.: 00062107) obtained from Sigma Aldrich, Germany. The MDCK-II cell line provides a perfect model to study wound closure processes because of their well-defined cell junctions and rapid growth. Additional information on the cell properties can be found elsewhere³³. The cell line was cultured as an adhesive monolayer in the medium MEM Earle's (Biochrom GmbH, Berlin, Germany) supplemented with 10 % fetal bovine serum (FPS

Superior) and 1 % Pen/Strep (Biochrom GmbH, Berlin, Germany) in NuncTM cell culture flasks (ThermoFisher Scientific, MA, USA) and in a saturated atmosphere with 5 % CO₂ at $T = 37$ °C. Cell passaging followed the standard trypsinization procedure using 1 ml Trypsin/EDTA (0,25 %) solution and PBS (w/o Ca²⁺, w/o Mg²⁺) (Biochrom GmbH, Berlin, Germany). Cell density was adjusted to 80.000 cells per 100 μ l.

Wound healing assay

The wound-healing assay provides the possibility to *in situ* monitor the progressive cell migration of two opposing confluent cell layers into a cell-free area. To obtain standardized starting conditions such as confluency, cell density or the width of the cell-free area, a commercially available silicone chamber assay was used. This so called culture insert (CI) (Ibidi[®] GmbH, Martinsried, Germany; width 500 μ m +/- 50 μ m) consists of two chambers with one adhesive side as illustrated in Fig. 1. a-1). Upon confluency, an artificial 'wound' in a confluent cell layer can be created upon its removal. After a short delay, cells at the edges of the confluent layers subsequently start to migrate into the empty gap at a constant speed³⁴.

Cell detachment assay

We also investigate the detachment of cells once they have formed a continuous layer on the sensitive area of the chip. In order to avoid fluctuations in the SAW S-parameters caused by changes of the covering fluid, cell-lysis substances Triton X-100 ($c = 0,05$ %) (T8787) or Terg-a-zyme[®] enzyme detergent ($c = 2,5$ g/l) (Z273287) (both Sigma-Aldrich, St. Louis, MO, USA) are added to the media. Furthermore, the cells were removed by apoptosis induced by heat shock ($T \geq 42$ °C).

Molality assay

In order to validate the dependence of the SAW S-parameters on the current molal concentration c_{Osm} of the cover fluid, the molality was measured while evaporating the nutrient on the SAW-chip. The molality c_{Osm} of a $V = 50$ μ l sample was determined with a freezing point osmometer (Osmomat3000, Gonotec GmbH, Berlin, Germany) at distinct time points.

Experimental setup

The above described SAW-chip was mounted on an in-house made sample holder (Fig. 1 A-1 c)) and contacted by a silver conducting paste (Acheson Silver DAG 1415M,

Acheson Industries Inc., MI, USA). To hold the culture nutrient and to house the cells, a polydimethylsiloxane (PDMS) chamber ($V = 3$ ml) (Sylgard 184 Silicone Elastomer, Dow corning, Germany; m/m ratio 10:1) was placed on top of the SAW-chip. Depending on the desired configuration, the disposable CI was placed either covering the IDTs aperture and delay line (Configuration 1 (C1)) or only covering the delay line (Configuration 2 (C2)) as shown in Fig. 1 A-2). In the following, 80.000 cells in $100 \mu\text{l}$ cell suspension were seeded into each chamber of the CI and filled with media after cell adhesion. After reaching confluency, the CI was removed, the cell layer washed with PBS and the chamber refilled with $V = 3$ ml fresh nutrient. To sustain optimal growth conditions (saturated atmosphere with 5 % CO_2 at $T = 37^\circ\text{C}$) the complete setup was placed into a microscope incubator (HT-200, ibidi, Munich, Germany) with an attached gas incubation system (The Brick, Live Image Services, Basel, Switzerland).

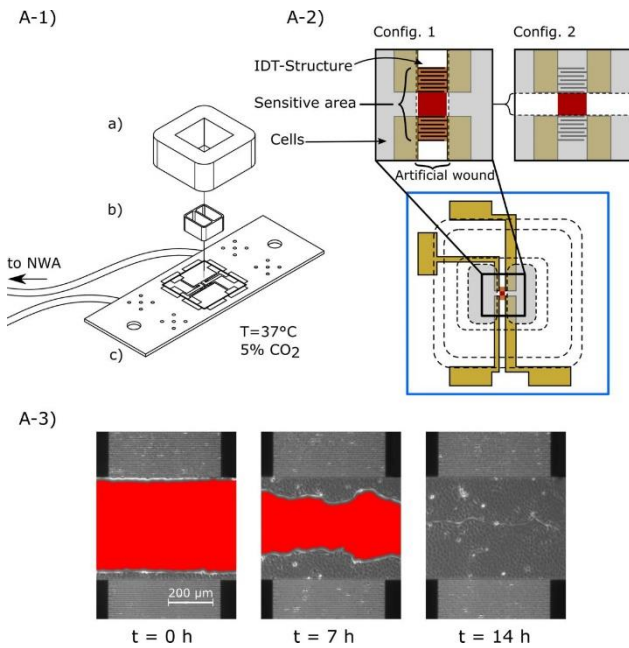


Fig. 1: A-1) Sketch of the experimental setup. Left: Exploded-view of the main components with (a) PDMS-chamber (b) CI and (c) sample holder with SAW-chip. A-2) Top-view of the SAW-chip showing the positioning of the components. Enlarged is the area of the delay line and the IDTs, which together form the sensitive area of the measurement and are located within the artificial wound in two configurations. A-3) Temporal evolution of a wound-healing process (red: cell free area).

Data acquisition and analysis

For our measurements, we use a 2-port vector network analyzer (ZVL, Rhode & Schwarz GmbH, Munich, Germany). The power of the sensing frequency sweep is set to $P = -10$ dBm.

By employing the time-gating function, the majority of adverse signals like crosstalk, edge reflections, triple transit signal and bulk waves can be eliminated. By applying this filtering-type operation in the Fourier-transformed time domain of the signals response, one obtains a largely noise-reduced signal when performing the back-transformation. This technique allows to accurately read out both amplitude and phase information of the SAW transmission signal.

A homemade LabVIEW (National Instruments, Austin, TX) software was used to read out the scattering (S)-parameter matrix. Here, the amplitude and phase of the reflection coefficients S_{11}, S_{22} and the forward gain S_{21} were recorded every 2.5 minutes for wound healing assays and every 15 seconds for cell detachment assays. While the phase change is measured at constant frequency, the amplitude values represent the current extreme values. This way, changes in the resonance frequency due to, e.g., mass loading effects are nicely compensated. The subsequent data analysis concerns the relative change in the amplitude ΔS and phase $\Delta\phi$ at time t compared to the value at the beginning of the experiment at $t = 0$.

The migration process into the cell-free area was optically observed with a microscope (Olympus CKX 41, Olympus Europa SE & Co. KG, Hamburg, Germany). Phase contrast images were taken every five minutes with a 5x (for C1), and 10x (for C2) objective, respectively. Phase contrast images at distinct time points at the beginning ($t = 0$ h), during ($t = 7$ h) and at the end ($t = 14$ h) of the experiment are shown in Fig. 1 A-3).

The cell-free area $A(t)$ was then analyzed semi-automatically using the modified ImageJ macro "MRI-Wound-Healing tool" (http://dev.mri.cnrs.fr/projects/imagej-macros/wiki/Wound_Healing_Tool) and, if necessary, manually corrected. The determined values $A(t)$ at t are standardized to the area at the beginning of the experiment $A(t = 0)$: $A_{\text{mig}}(t) = \frac{A(t)}{A(0)}$. The normalized cell free area $A_{\text{mig}}(t)$ is then plotted as function of the elapsed time.

Simulation

Finite element method (FEM) simulations were performed using the commercially available software COMSOL Multiphysics (5.0) (Comsol Inc., Burlington, MA, USA). For the time dependent studies as well as for the eigenfrequency studies, the Piezoelectric Devices Module was used. The model geometry of the eigenfrequency study is reduced to the periodic unit cell, where the width, depth and height of the substrate equals $\lambda, \lambda/8$

and 5λ , respectively. Periodic boundary conditions were used along both vertical boundaries of the geometry. The lower boundary is fixed, which enforces a zero structural displacement. All other boundaries are left to the default boundary conditions, which are “Free” for the Solid Mechanics interface and “Zero Charge” for the Electrostatics interface, respectively. Instead of rotating the substrate we used a rotated coordinate system (Euler angle: $0^\circ, 54^\circ, 0^\circ$) to get the right crystal orientation of 36° -YX Lithium Tantalate. Like in the experiment, the substrate in the simulation is covered with a 150 nm thick SiO_2 film, which in the model is represented by a linear elastic material. The properties of the material are its Young’s modulus $E = 70.55$ GPa, its poisson ratio $\nu = 0.17$, its density $\rho = 2410$ kg/m³ and its relative permittivity $\epsilon_r = 3.9$. On top of the SiO_2 film, three layers with heights of 100 nm (layer 1), 10 μm (layer 2) and 40 μm (layer 3) are built, representing the cell culturing media (layer 1 and 3) and the cells (layer 2) themselves. Based on perturbation theory, only the electric properties of the various layers are considered in the model as explained below. To represent permittivity as well as conductivity changes in the simulation, a complex permittivity $\hat{\epsilon}_r$ is introduced to the model:

$$\hat{\epsilon}_r = \epsilon_r' - i\epsilon_r'' = \epsilon_r - i\frac{\sigma}{\omega}$$

Here, ϵ_r denotes the real part of the permittivity for static fields, σ the conductivity and ω the frequency. A mapped mesh with maximum mesh size of 2.5 μm was added to the entire geometry. The substrate for our time dependent studies has a height of $h = 100$ μm and a length of $l = 300$ μm , which corresponds to 5λ and 15λ . In order to reduce the computation time, periodic boundary conditions with continuity are assumed along the y-axis. This is equivalent to an infinite long substrate and thereby an infinite IDT aperture. Furthermore, any possible influences of reflections by outgoing waves at the sides and bottom of the substrate are minimized due to low reflecting boundary conditions. The transmitter and receiver IDT (two finger pairs each) are placed at a distance of 100 μm to each another. The width of the fingers of the electrodes and also the distance between them is chosen to be 5 μm , which results in a wavelength $\lambda = 20$ μm . The first and third electrode of the input IDT have a potential boundary condition, whereas the second and fourth electrode are grounded. To receive a signal at the output IDT the first and third electrode are set as a floating potential and the second and fourth electrode are grounded. On top of the substrate, the same configuration as for the eigenfrequency study was used.

The cell free area on the delay line is varied, while the remaining of the substrate is permanently covered. For the time dependent simulations, a voltage signal of the form $U(t) = U_0 \sin(2\pi ft)$ with $U_0 = 1$ V and frequency $f = 208$ MHz is applied to the input IDT for 14.4 ns. The time step is set to $\Delta t = 0.2$ ns with results in a total simulation time of $t = 55$ ns. A more detailed description of the theoretical background and the model geometry of the simulation can be found in the SI.

RESULTS AND DISCUSSION

Effect of cell spreading and adhesion on SAW propagation

The above described acoustic SAW sensor is sensitive to changes in the mechanical (e.g. mass-loading and viscosity) and electrical properties (e.g. conductivity, permittivity) taking place within the sensor’s penetration depth δ^7 . Although the transmission signal typically serves as measure for sensor applications, all accessible parameters are shown in the following. Apart from the transmission, this also includes the reflection of the IDT-structures. Here, the parameters for both configurations are displayed to gain an overview of the typical respective progressions.

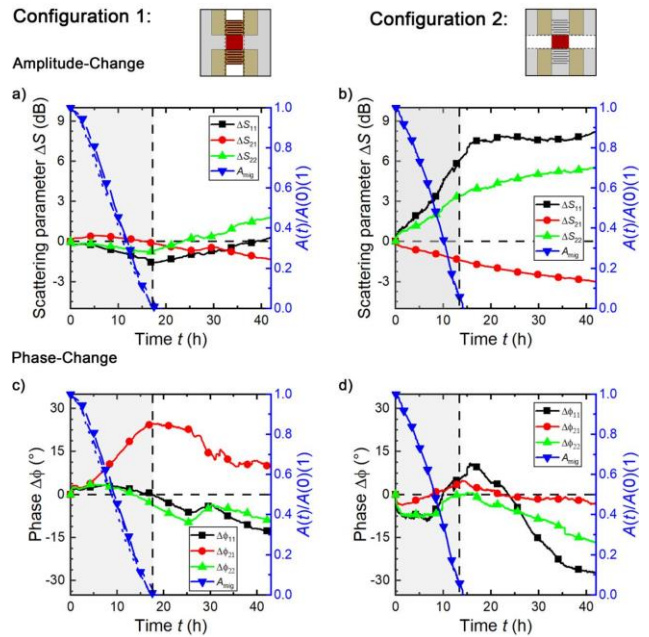


Fig. 2: Temporal development of the SAW S-parameters during (gray shaded) and after a wound-healing process. Amplitude (a, b) and phase (c, d) variance for C1 (left) and C2 (right). Data: C1-2 and C2-2. Color code in the schematic representation of C1 and C2: red: sensitive area, white: cell-free area, gray: cell covered area.

The acquired data of the amplitude- (ΔS) (a, b) and phase- ($\Delta \phi$) (c, d) change of the S-parameters during a wound-healing process and after the wound closure for selected

examples are displayed in Fig. 2. These shown data are representative for all performed experiments. The blue graphs are displaying the normalized cell-free area $A_{\text{mig}}(t)$ (as being optically determined) at the delay line (solid) and additionally for C1 at IDT-1 (dashed) and IDT-2 (dotted). The grey shaded area marks the time period of wound closure and thus changes in the cell-free area.

In order to enable a quantitative assessment at which point in time the wound is completely closed or the migration has stopped, the temporal development of the measured S-parameters must correlate with $A_{\text{mig}}(t)$ and should show a distinct change in the signals temporal evolution. This includes for example a pronounced extreme value (maximum or minimum) or steady state after the complete wound closure.

For C1, the variation ΔS of both reflection coefficients S_{11} and S_{22} are slightly decreasing during cell coverage while ΔS_{21} remains nearly constant (Fig. 2. a)). Upon complete wound closure, a clear minimum for ΔS_{11} and ΔS_{22} is visible but not for ΔS_{21} . Considering the phase $\Delta\phi$ in Fig. 2 c, there is no significant effect for $\Delta\phi_{11}$ or $\Delta\phi_{22}$, but $\Delta\phi_{21}$ undergoes a strong change instead. Following a similar trend to $A_{\text{mig}}(t)$, the maximum value of $\Delta\phi_{21} = 24,8^\circ$ is reached exactly at the point of wound closure. The positive increase of $\Delta\phi_{21} > 0$ indicates an increase of the SAWs velocity v .

Considering C2, surface coverage related changes in the amplitude ΔS are apparent but not simply to be assigned to $A_{\text{mig}}(t)$, as shown in Fig. 2 b). Analog to C1, the variation of the phase $\Delta\phi$ in C2 correlates significantly with the cell free area (Fig. 2 d)). While $\Delta\phi_{11}$ and $\Delta\phi_{22}$ are slightly shifted in time and not exactly on the point of wound-closure, $\Delta\phi_{21}$ corresponds perfectly with $A_{\text{mig}}(t)$ though. Among all parameters, $\Delta\phi_{21}$ in C2 shows the highest conformity with $A_{\text{mig}}(t)$.

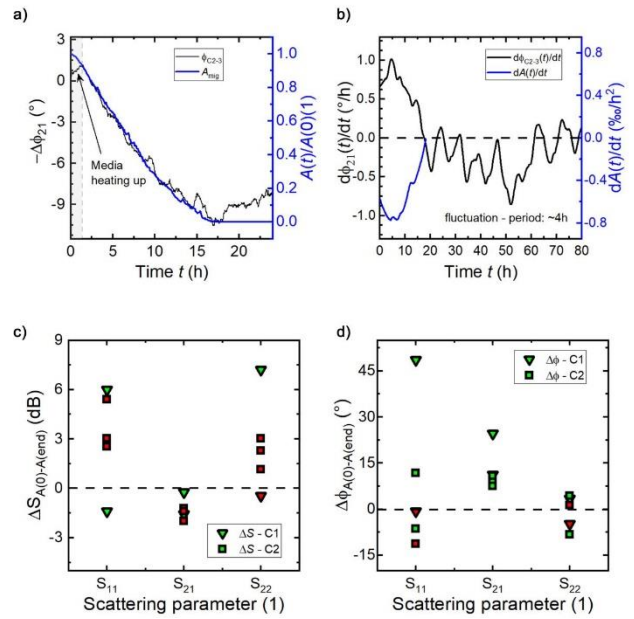


Fig. 3: a) Correlation of the phase shift $\Delta\phi_{21}$ and the normalized cell free area $A_{\text{mig}}(t)$ in C2. b) First derivative of ϕ_{21} and $A(t)$. The first zero crossing of $\dot{\phi}(t)$ and $\dot{A}_{\text{mig}}(t)$ at the same time point marks the total wound closure. Emerging fluctuations for $t > 19$ h. Overview of the amplitude- (c) and phase- (d) change from the start ($t=0$) to total wound closure ($t=t_{\text{end}}$) of all performed experiments in both configurations. The colour of the inner symbol areas marks the existence of an extreme value with green = true and red = false. Data a)/b): C2-3.

The strong correlation between $\Delta\phi_{21}$ and $A_{\text{mig}}(t)$ in C2 is shown in Fig. 3 a). Unaffected by the high sensitivity caused fluctuations, the main course of $\Delta\phi_{21}$ matches with a high accordance the course of $A_{\text{mig}}(t)$. At the beginning for $0 \text{ h} < t < 1 \text{ h}$ and indicated by the arrow, the temperature equilibration of the fresh nutrient is measurable by causing an increase of $\Delta\phi_{21}$. Both the first derivatives $\dot{\phi}(t)$ and $\dot{A}_{\text{mig}}(t)$ (see (Fig. 3 b)) exhibit an identical course for their absolute values. The first zero crossing here marks the time point of complete wound closure. For $t > 19 \text{ h}$ after the wound closure, $\dot{\phi}(t)$ begins to oscillate with a period of about 8 hours.

In order to achieve a high significance, several experiments were performed and evaluated for each configuration. Comparing all performed experiments in Fig. 3 c) and d), the measured values ΔS_{11} , ΔS_{22} , $\Delta\phi_{11}$ and $\Delta\phi_{22}$ exhibit a quite wide distribution and the relative difference of ΔS_{21} turns out to be too small for both C1 and C2.

In contrast, $\Delta\phi_{21}$ turns out to be ideally suited for the desired sensing application. Considering the presence of a distinct change in the time evolution, as indicated by the colour of the inner symbol areas (red = false / green = true), only $\Delta\phi_{21}$ in C2 can surely be assessed to

determine changes in the cell-free area $A_{\text{mig}}(t)$ with a mean value of $\Delta\bar{\phi}_{21} = 9,6^\circ \pm 1,7^\circ$.

This can be understood by the migration direction. While in C1 cells are invading the sound path laterally, cells in C2 are migrating along the sound path. This makes it possible for C2 to distinguish the perturbation length l between “uncovered” l_l (l: liquid) and “covered” l_c (c: cells), but not for C1. Therefore, the SAW is propagating both in a cell covered section and a section without cells. The phase shift can thus be compared to the fractional change $\frac{l_c}{l_l+l_c}$.

In C1, during the cell migration, the phase shift is a superposition of SAW propagating on a cell free and a cell covered area. Moreover, as the IDTs themselves are not covered in the beginning of the experiment, the total sensitive area is up to four times larger ($0.91 \text{ mm}^2 : 0.25 \text{ mm}^2$), leading to larger absolute values of $\Delta\phi_{21}$ as compared to C2 and shown in Fig. 3 d) for one measurement. However, $\Delta\phi_{21}$ is subjected to larger fluctuations, if the sensitive area is not uniformly covered by the invading cell front. Thus, we suggest the C2 configuration as the most promising experimental design.

Quantifying cell detachment and nutrient quality

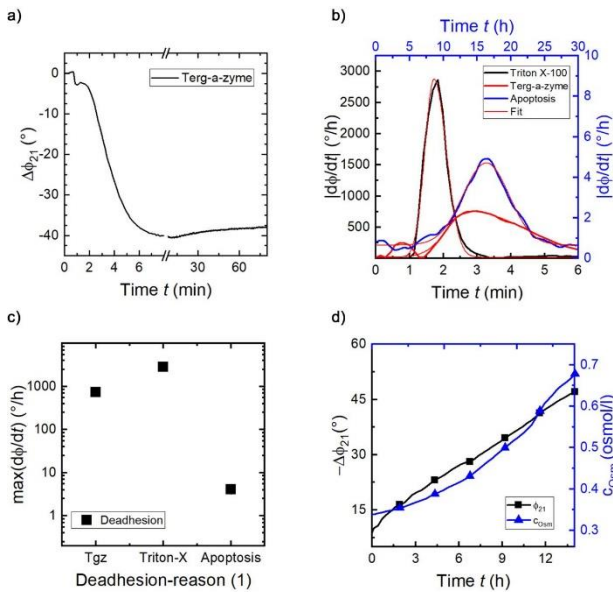


Fig. 4: a) Temporal development of $\Delta\phi_{21}$ during the detachment and lysis of a confluent cell layer. b) First derivatives of the detachment kinetics for different cell lysis origins. c) Comparison of the detachment efficiency. d) Phase shift of $\Delta\phi_{21}$ due to changes in the molality c_{Osm} .

Beyond the dynamic cell invasion into the cell free area, our proposed sensor is also able to measure the detachment process of a confluent cell layer initially covering the sensing area. Fig. 4 a) displays the phase shift $\Delta\phi_{21}$ during such a detachment process. As

expected, the development of $\Delta\phi_{21}$ is opposing the covering process shown in Fig. 3 d) with $\Delta\phi_{21} < 0$ indicating a decrease of v . The total average change $\Delta\bar{\phi}_{21} = -41,44^\circ \pm 5,9^\circ$ is larger, though. Compared to $\Delta\phi_{21}$ for C2, the total change in $\Delta\phi_{21}$ is up to four times larger for the detachment process than for the covering process. Again, this can be understood by comparing the areas of the IDTs and the cell free area at the beginning of the experiment. As only the delay line is affected in C2 by the covering process due to cell migration, the whole sensitive area including the IDTs is influenced by the detachment event. Then, with an almost four times larger sensitive surface (IDT-1, IDT-2, delay line) as compared to the delay line itself, the surface ratio corresponds to the ratio of the total phase shift.

Furthermore, the duration of the process is strongly dependent on the origin and cause of the detachment. For a quantification of the detachment kinetics, the first derivatives of ϕ_{21} are plotted in Fig. 4 b). Assuming a normal distribution of the processes, the data are approximated by a bi-gaussian fit function. The rate of the change described by $d\phi_{21}/dt$ provides insight into the effectiveness of the lysis process. Thus, it is possible to quantify the lysis efficiency by comparing the maximum values given by the fit function of $d\phi_{21}/dt$ as shown in Fig. 4 c).

As expected, cell lysis detergents like Terg-a-zyme or Triton X-100 indicate a many times higher detachment efficiency as compared to heat induced apoptosis.

Another advantage of the SAW sensor is the possibility to monitor the cultivation conditions. Apart from the wound healing assay, the sensor can also easily detect variations in the temperature³⁵, salt concentration³⁶ or pH-value³⁷. Besides the changes of $\Delta\phi_{21}$ caused by cell detachment and adhesion processes, the SAW phase is also shifted by changes in the molal concentration c_{Osm} of the surface covering fluid. Fig. 4 d) demonstrates a relation between c_{Osm} and $\Delta\phi_{21}$. With increasing molality c_{Osm} , the phase velocity v is decreasing, leading to a negative phase shift. The phase shift in Fig. 4 d) is therefore related to the increased conductivity of the medium. As the conductivity increases, the phase velocity decreases³⁶. Employing an additional delay line in the cell free area along the same lines as shown earlier³⁸ would allow for the definite separation of changes in the environmental conditions (temperature, pH, ion concentrations,...) and the actual change in cell coverage. However, this was not necessary here.

Simulation

In order to identify the effect off cell spreading and adhesion on SAW propagation, we used an

eigenfrequency study as well as a time dependent study with a simplified 3D model of the acoustic sensor used in the experiments. Earlier studies reported that SAW sensors are sensitive to electrical as well as mechanical changes leading to change in the phase velocity v . Kondoh et al. experimentally and theoretically demonstrated that under the influence of a liquid covering the chip, changes of the density ρ and viscosity η lead to a change of the fractional velocity³⁹:

$$\frac{\Delta v}{v} \propto -\Delta(\sqrt{\rho\eta}).$$

The product $\sqrt{\rho\eta}$ for the nutrient and cell uncovered surface can be approximated to $\sqrt{\rho_l\eta_l} \approx 0.1 \left[\left(\frac{\text{g}^2}{\text{cm}^4\text{s}} \right)^{0.5} \right]$ with ρ_l the density and η_l the viscosity of water. Janshoff and colleagues measured the product $\sqrt{\rho_c\eta_c}$ for MDCK-II cells⁴⁰: $\sqrt{\rho_c\eta_c} \approx 0.386 \left[\left(\frac{\text{g}^2}{\text{cm}^4\text{s}} \right)^{0.5} \right]$. Assuming the cell layer acting like a viscous liquid, an increase of $\sqrt{\rho\eta}$ leads to a decrease of the fractional velocity change. The minor changes in $\sqrt{\rho\eta}$ and the opposing trend to the experimental observations (v increases) practically exclude changes in mechanical properties as being the reason for the observed phase shift $\Delta\phi_{21}$. In the simulation, we therefore focused on the electrical properties of the covering material to explain the behavior of $\Delta\phi_{21}$. This approach appears to be reasonable, as the electromechanical coupling coefficient $K_s^2 = 2\Delta v/v_0$ is large for LiTaO₃ 36° YX-cut. The fractional velocity shift $\Delta v/v$ equals the fractional frequency shift $\Delta f/f$ and can be extracted from the eigenfrequency study. Furthermore, the phase shift is dependent on the perturbation length l , which can be separated into l_1 and l_c for the propagation in the cell uncovered and covered section in C2, respectively. For the fully closed wound, l_c equals the length of the delay line l_d . Assuming that the total phase shift $\Delta\phi_{21}$ for the fully closed wound is proportional to the fractional velocity shift and the ratio of the length of the delay line to the wavelength λ , we can make use of:

$$\Delta\phi_{21} = \frac{\Delta v}{v} \cdot \frac{l_d \cdot 360^\circ}{\lambda}.$$

In a first step, we looked at a simple model with only one overlaying material covering the surface to get a first qualitative insight how the electrical properties of an overlaying material influences the fractional velocity shift and thereby the sensor output $\Delta\phi_{21}$. The simulation results of this simplified model can also easily be verified by comparing it to theoretical models. Therefore, we compare the fractional velocity change $\Delta v/v$ from the

simulation with the perturbation technique introduced first by Auld et al.⁴¹. The fractional velocity change in dependence of the relative permittivity and conductivity of the covering material due to the acoustoelectric interaction can according to Kondoh et al. be calculated by:^{39,42}

$$\frac{\Delta v}{v} = \frac{K_s^2 (\sigma'/\omega)^2 + \epsilon_0(\epsilon_r' - \epsilon_r)(\epsilon_r'\epsilon_0 + \epsilon_p^T)}{2 (\sigma'/\omega)^2 + (\epsilon_r'\epsilon_0 + \epsilon_p^T)^2}.$$

Here, $K_s^2 = 0.028$ is the coupling coefficient, σ' the conductivity of the sample liquid, ϵ_0 the vacuum permittivity, ϵ_r' the permittivity of the sample liquid, $\epsilon_r = 80$ the permittivity of water, $\epsilon_p^T = 4.58 \cdot 10^{-10}$ F/m the effective permittivity and $\omega = 2\pi f$ with $f = 208.4$ MHz the resonance frequency.

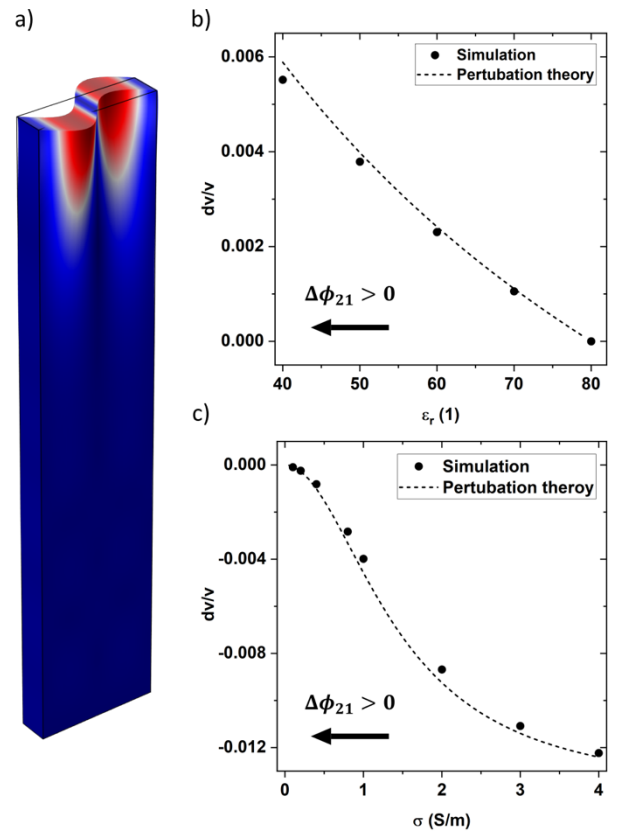


Fig. 5: a) Typical result of the eigenfrequency study. The colour code indicates the surface total displacement (no scale given: red high, blue low). The eigenmode clearly indicates the expected shear character of the wave. From the eigenfrequency studies the fractional velocity change in dependency of the relative permittivity (b) and conductivity (c) of the covering liquid is extracted. Dots show results from simulation and dashed line the perturbation theory.

Fig. 5 a) presents a typical result from the eigenfrequency study (the color code indicates the surface total displacement. No scale provided). The shown eigenmode clearly demonstrates the expected shear character of the wave. From the eigenfrequency study, the fractional velocity change can be extracted. Fig. 5 b and c show the

result from the simulation (dots) and the theory (dashed line) in dependency of the relative permittivity ϵ_r and conductivity σ of the covering material. For increasing permittivity as well as increasing conductivity, the fractional velocity shift decreases. The simulated data are in very good agreement with the theory. In the experiment, we see an increase of $\Delta\phi_{21}$ while the gap in the cell layer is being closed. Referring to the results of both the simulation and the theory, this means that the permittivity and conductivity of the cells has to be lower than the one of the cell culturing media. We thus used two theoretical approaches to determine the permittivity values. According to Li et al.⁴³ the permittivity of an electrolyte solution can be calculated by combining the classical Debye and the Drude model. For the cell culturing media, we obtain a value of $\hat{\epsilon}_r = 80 - i123$. For the description of the cells, we used the double-shell model described by Pehrig⁴⁴. Here, we obtain values ranging from $\hat{\epsilon}_r = 50 - i71$ to $\hat{\epsilon}_r = 55 - i120$, depending on the fractional volume r of the cell occupied by the nucleus (for details to both methods see the SI). Because the real part as well as the imaginary part of the calculated permittivity of the cells is lower than the value of the cell culturing media, we can conclude that the increase of $\Delta\phi_{21}$ is in accordance to the findings of this simplified model.

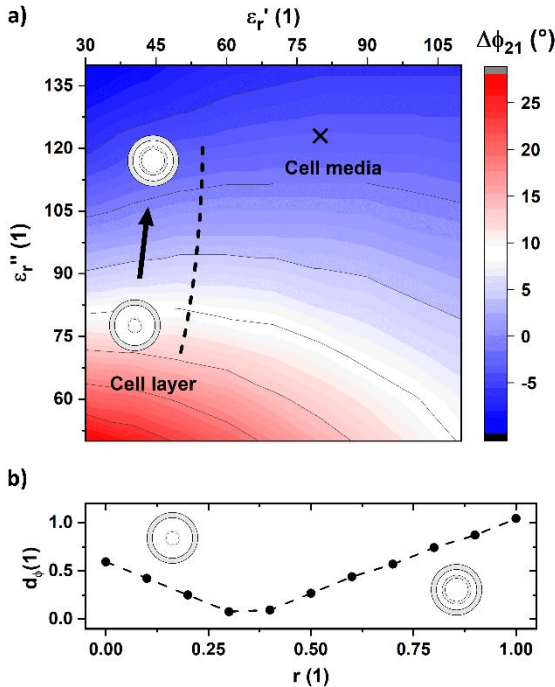


Fig. 6: a) Phase shift $\Delta\phi_{21}$ in dependence of the real and imaginary part of the permittivity. The phase shift is calculated relative to the cell culturing media ($\hat{\epsilon}_r = 80 - i123$). The dashed line indicates the different values of the permittivity for increasing fractional volume r of the cell occupied by the

nucleus. b) Relative difference of the phase shift experiment to simulation d_ϕ depending on the volume fraction r . A minimum of d_ϕ is observed for a values of $r \approx 0.3$.

In a next step, instead of only one single layer, we used the configuration with a thin water layer being present between sensor surface and cell layer, as described in the materials and methods part, which is closer to the experiment. The intention of this more realistic model is now to also quantitatively describe the behavior of $\Delta\phi_{21}$. Fig. 6 a) presents the phase shift $\Delta\phi_{21}$ in dependence of the real and imaginary part of the permittivity ϵ'_r and ϵ''_r . The phase shift is calculated relative to the cell culturing media ($\hat{\epsilon}_r = 80 - i123$). Starting from the cell media, a decrease of ϵ'_r and ϵ''_r always leads to an increase of $\Delta\phi_{21}$. This observation is consistent with the findings of the one-layer model. The dashed line indicates the theoretical values of the permittivity for increasing fractional volume r of the cell occupied by the nucleus. Fig. 6 b) shows the relative difference d_ϕ of the phase shift obtained in the simulation to the values of the experiment ($\Delta\phi_{21} \approx 10^\circ$). A minimum of d_ϕ is obtained for $r \approx 0.3$. The permittivity of the cell layer is thereby best described in the simulation, with a value of $\hat{\epsilon}_r = 52 - i84$.

Oscillations after Wound Closure

As shown above, upon the full closure of the cell layer, obvious periodic fluctuations of $\Delta\phi_{21}$ with an apparent period of 8 h are emerging in the experiment, indicating some periodic changes of the boundary conditions for SAW propagation. Zehnder et al., for instance, identified cell volume fluctuations in MDCK monolayers⁴⁵. According to this study, and depending on the cytoskeletal activity, the cell volume oscillates with an amplitude of about 20% at a timescale of 4h. As the size of the nucleus stays constant, the ratio r changes with the volume change. This affects the effective permittivity of the cell layer and therefore the phase shift $\Delta\phi_{21}$. Such fluctuations of r induced by cytoskeletal activity could therefore well explain the observed oscillatory behavior of the derivative of $\Delta\phi_{21}$ for $t > 20$ h. Fluctuations in the Love-wave signal by a cell covered surface were also observed by Wu et al. for stem/progenitor cells. Here they claim that a change in cellular mechanical properties like the storage or shear modulus of the cytoskeleton lead to a pronounced and characteristic variation in the signal²³.

Role of the cell-sensor distance

Another hypothesis would be that the cell-surface distance varies when the cells cannot migrate anymore. The cell layer density increases due to cell proliferation, leading to dome formations. To prove this hypothesis, the influence of cell-surface distance was also investigated in our simulations. Fig. 7 shows $\Delta\phi_{21}$ for different distances h . For low values of $h < 100\text{nm}$, $\Delta\phi_{21}$ stays nearly constant. In the range of $100\text{nm} < h < 10\mu\text{m}$, $\Delta\phi_{21}$ drops rapidly down to zero. For larger h values, $\Delta\phi_{21}$ stays at this level. This result shows that the sensor can detect changes near the surface in the region up to half of the wavelength. Above this value, $\Delta\phi_{21}$ is no longer significantly influenced by changes in the electrical environment. Furthermore, as the cell-surface distance during migration is typically around 100nm , it seems plausible that changes of h will influence the sensor output $\Delta\phi_{21}$ as it is highly sensitive in this region. Thus, the hypothesis of a change of the cell-sensor distance h after reaching confluency is also consistent with the observation that $\Delta\phi_{21}$ decreases from this point on in the experiment.

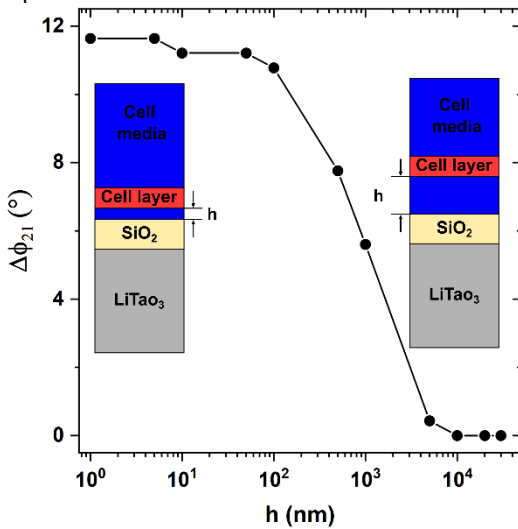


Fig. 7: $\Delta\phi_{21}$ for different cell-substrate distances h . For low values of h , $\Delta\phi_{21}$ is nearly constant. In the range of $100\text{nm} < h < 10\mu\text{m}$, $\Delta\phi_{21}$ drops rapidly down to zero.

In addition to the eigenfrequency study, we performed a time dependent study. The model consists of a transmitter and receiver represented by two finger-pair electrodes, which allows us to generate and detect SAW. The transmitter electrodes are supplied with a sinusoidal voltage signal having an amplitude $U_0 = 1\text{ V}$ and being applied for a time period of $t = 14.4\text{ ns}$ and a frequency $f = 208\text{ MHz}$. Fig. 8 a) shows the surface total displacement (xz -plane, colour code not provided). Two waves in $-x$ and x direction are generated. The top view (xy -plane) clearly again shows the quasi-shear character of the wave. The mechanical wave leads to an rf voltage signal

at the receiver electrodes because of the piezoelectric effect (Fig. 8 b and c). The gray shaded area up to 15 ns is an interference signal caused by capacitive crosstalk between transmitter and receiver. Since it is clearly separated in time from the actual SAW signal (30 ns to 50 ns), it is irrelevant here. $\Delta\phi_{21}$ is calculated from the time lag between the signals as follows:

$$\Delta\phi_{21} = 5 \cdot \frac{\Delta t}{T} \cdot 360^\circ,$$

with Δt the time difference between the signals and T the period time. The prefactor 5 accounts for the five times longer delay line in the experiment compared to the simulation. In Fig. 8 d), we demonstrate the dependence of $\Delta\phi_{21}$ on the cell free area A_{mig} . For a fully covered surface, a maximum value of $\Delta\phi_{21} = 16^\circ$ is observed. The simulations furthermore indicate a linear relation of $\Delta\phi_{21}$ and A_{mig} . This observation is consistent with the experiment, likewise.

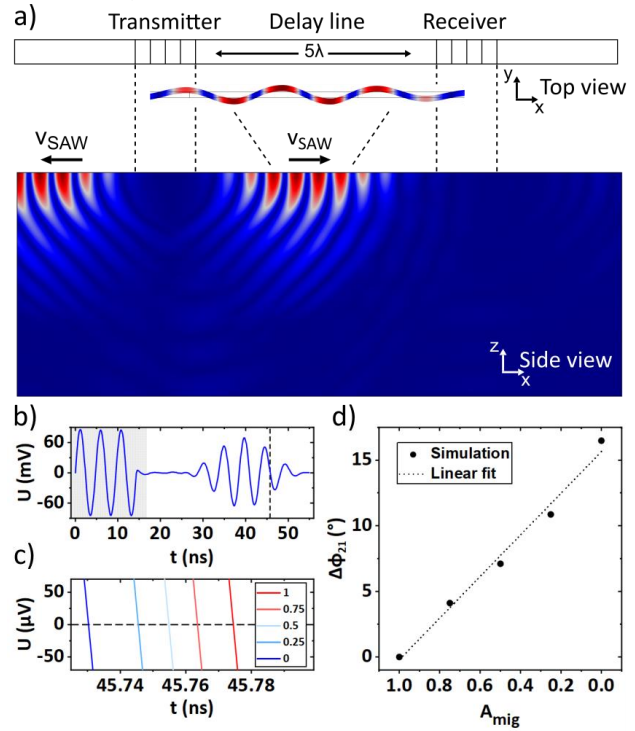


Fig. 8: a) Total surface displacement (xz -plane) resulting from time dependent simulations. The generated pulse is traveling from left to right and is detected at the receiver. The top view (xy -plane) clearly shows the quasi-shear character of the wave. b) Detected rf voltage signal U at the receiver as a function of time t for different values of A_{mig} . The phase shift $\Delta\phi_{21}$ is calculated from the time lag between the signals. c) $\Delta\phi_{21}$ shows a linear behavior in dependence of A_{mig} .

Employing FEM simulations, we showed that the electric properties of the surface covering cells and the nutrient strongly influences the phase velocity. An eigenfrequency as well as a time dependent study with a simplified model geometry was used to estimate the behavior of $\Delta\phi_{21}$, which is detected in the experiment. Both methods have the power to predict the total phase shift for a fully

closed wound. However, there is a phase deviation of a few degrees between both methods. However, considering the assumptions that were made in the simulation, especially for the calculation of the electric properties of the cell layer, both methods are close enough to the values observed in the experiment. With the eigenfrequency study, which is less time consuming than the time dependent study, it is thus possible to vary model input parameter over a wider range. The time dependent study is closer to the configuration in the experiment. Here the linear behavior of $\Delta\phi_{21}$ for C2 during the wound healing process could be confirmed (see Fig. 8).

CONCLUSION AND OUTLOOK

In this study, we open up several new application fields for SAW based sensors. Our results clearly demonstrate the capability of SAW sensors for the analysis of a standardized wound-healing assay without the need of microscopy observation.

In the SAW sensor experiments, we measured the phase velocity shift due to the presence of biological layers on the sensing surface. The phase shift $\Delta\phi_{21}$ strongly correlates with the change in the cell covered surface $A_{\text{mig}}(t)$. As an additional, unprecedented application, we showed the ability to measure detachment kinetics as a consequence of cell death by apoptosis or necrosis. Moreover, our setup allows to quantify the cell lysis ability of a substance by the change in $\Delta\phi_{21}$ as a reliable parameter. But not only the healing process can be observed, but also cell growth like cytoskeletal activity. The demonstrated data and our experimental findings are supported by FEM simulations, allowing to predict $\Delta\phi_{21}$ for different configurations. Using eigenfrequency and time dependent studies, cellular processes can be represented and future setup design to be optimized.

Depending on the required sensitivity and selectivity, the chosen SAW-Chip design could be further improved and specified. Using a combination of metal-coated and metal-free surfaces, for example, electrical changes like the ones being caused by permittivity and conductivity variations can be separated from changes in the mechanical properties.

Employing a larger thickness of the SiO₂ layer, more acoustic energy is confined at the surface. This causes an improved sensitivity to changes in the properties of the material on top of the sensor. Moreover, using so called Split-IDTs operating at different frequencies would allow sensing at slightly different penetration depths. This might allow to sense the cell-surface binding process separately from the cell coverage.

ACKNOWLEDGMENTS

The authors would like to acknowledge funding by Nanosystems Initiative Munich (NIM), the Center for NanoScience (CeNS), the "Studienstiftung des deutschen Volkes", "WiR - Wissenstransfer Region Augsburg" and the Augsburg Centre for Innovative Technologies (ACIT).

REFERENCES

1. Stamp, M. *et al.* Exploring the Limits of Cell Adhesion under Shear Stress within Physiological Conditions and beyond on a Chip. *Diagnostics* **6**, 38 (2016).
2. Jötten, A. M. *et al.* Correlation of in vitro cell adhesion, local shear flow and cell density. *RSC Adv.* **9**, 543–551 (2019).
3. Saitakis, M. & Gizeli, E. Acoustic sensors as a biophysical tool for probing cell attachment and cell/surface interactions. *Cell. Mol. Life Sci.* **69**, 357–371 (2012).
4. Fang, Y. Label-Free and non-invasive biosensor cellular assays for cell adhesion. *Surf. Interfacial Asp. Cell Adhes.* 155–165 (2011). doi:10.1163/016942409X12598231568267
5. Hug, T. S. Biophysical Methods for Monitoring Cell-Substrate Interactions in Drug Discovery. *Assay Drug Dev. Technol.* **1**, 479–488 (2003).
6. Tiruppathi, C., Malik, A. B., Del Vecchio, P. J., Keese, C. R. & Glaever, I. Electrical method for detection of endothelial cell shape change in real time: Assessment of endothelial barrier function. *Proc. Natl. Acad. Sci. U. S. A.* **89**, 7919–7923 (1992).
7. D. Ballantine, J. R. W. S. M. A. R. E. Z. G. F. H. W. *Acoustic Wave Sensors.* (Academic Press, 1997).
8. Wohltjen, H. Mechanism of operation and design considerations for surface acoustic wave device vapour sensors. *Sensors and Actuators* **5**, 307–325 (1984).
9. Gryte, D. M., Ward, M. D. & Hu, W. -S. Real-Time Measurement of Anchorage-Dependent Cell Adhesion Using a Quartz Crystal Microbalance. *Biotechnol. Prog.* **9**, 105–108 (1993).
10. Lord, M. S. *et al.* Monitoring cell adhesion on tantalum and oxidised polystyrene using a quartz crystal microbalance with dissipation. *Biomaterials* **27**, 4529–4537 (2006).
11. Redepenning, J., Schlesinger, T. K., Mechalke, E. J., Puleo, D. A. & Bizios, R. Osteoblast Attachment Monitored with a Quartz Crystal Microbalance. *Anal. Chem.* **65**, 3378–3381 (1993).
12. Wegener, J., Janshoff, A. & Galla, H. J. Cell adhesion monitoring using a quartz crystal microbalance comparative analysis of different mammalian cell lines. *Eur. Biophys. J.* **28**, 26–37

- (1998).
13. Wegener, J., Seebach, J., Janshoff, A. & Galla, H. J. Analysis of the composite response of shear wave resonators to the attachment of mammalian cells. *Biophys. J.* **78**, 2821–2833 (2000).
 14. Modin, C. *et al.* QCM-D studies of attachment and differential spreading of pre-osteoblastic cells on Ta and Cr surfaces. *Biomaterials* **27**, 1346–1354 (2006).
 15. Kovacs, G., Lubking, G. W., Vellekoop, M. J. & Venema, A. Love waves for (bio)chemical sensing in liquids. *Proc. - IEEE Ultrason. Symp.* **1992- Octob**, 281–285 (1992).
 16. Gizeli, E., Goddard, N. J., Lowe, C. R. & Stevenson, A. C. A Love plate biosensor utilising a polymer layer. *Sensors Actuators B. Chem.* **6**, 131–137 (1992).
 17. Stamp, M. E. M., Brugger, M. S., Wixforth, A. & Westerhausen, C. Acoustotaxis: In vitro stimulation in a wound healing assay employing surface acoustic waves. *Biomater. Sci.* **4**, (2016).
 18. Brugger, M. S. *et al.* Vibration enhanced cell growth induced by surface acoustic waves as in vitro wound healing model. *PNAS* accepted 2020
 19. Greco, G. *et al.* Surface-Acoustic-Wave (SAW)-Driven Device for Dynamic Cell Cultures. *Anal. Chem.* **90**, 7450–7457 (2018).
 20. Stamp, M. E. M. *et al.* Acoustic Streaming Driven Enhanced Dye-Uptake in Cells for Fluorescence Imaging. in *2018 IEEE International Ultrasonics Symposium (IUS)* 206–212 (IEEE, 2018). doi:10.1109/ULTSYM.2018.8579948
 21. Ramesan, S., Rezk, A. R., Dekiwadia, C., Cortez-Jugo, C. & Yeo, L. Y. Acoustically-mediated intracellular delivery. *Nanoscale* **10**, 13165–13178 (2018).
 22. Gronewold, T. M. A. Surface acoustic wave sensors in the bioanalytical field: Recent trends and challenges. *Anal. Chim. Acta* **603**, 119–128 (2007).
 23. Wu, H., Zu, H., Wang, J. H.-C. & Wang, Q.-M. A study of Love wave acoustic biosensors monitoring the adhesion process of tendon stem cells (TSCs). *Eur. Biophys. J.* **48**, 249–260 (2019).
 24. Furniss, J., Qin, L., Ng, S., Voiculescu, I. & Li, F. Love mode surface acoustic wave and impedance sensors for water toxicity sensing. *Environ. Prog. Sustain. Energy* **37**, 172–179 (2018).
 25. Saitakis, M., Tsortos, A. & Gizeli, E. Probing the interaction of a membrane receptor with a surface-attached ligand using whole cells on acoustic biosensors. *Biosens. Bioelectron.* **25**, 1688–1693 (2010).
 26. Zhang, X. *et al.* A novel sensitive cell-based Love Wave biosensor for marine toxin detection. *Biosens. Bioelectron.* **77**, 573–579 (2016).
 27. Higashiyama, T. *et al.* Detection of cellular damage by hydrogen peroxide using SV40-T2 cells on shear horizontal surface acoustic wave (SH-SAW) sensor. *Ultrasonics* **54**, 1430–1438 (2014).
 28. Morgan, D. *Surface Acoustic Wave Filters, 2nd Edition.* (Academic Press, 2007).
 29. Länge, K., Rapp, B. E. & Rapp, M. Surface acoustic wave biosensors: A review. *Anal. Bioanal. Chem.* **391**, 1509–1519 (2008).
 30. White, R. M. & Voltmer, F. W. Direct piezoelectric coupling to surface elastic waves. *Appl. Phys. Lett.* **7**, 314–316 (1965).
 31. Martin, F., Newton, M. I., McHale, G., Melzak, K. A. & Gizeli, E. Pulse mode shear horizontal-surface acoustic wave (SH-SAW) system for liquid based sensing applications. *Biosens. Bioelectron.* **19**, 627–632 (2004).
 32. Saitakis, M., Dellaporta, A. & Gizeli, E. Measurement of two-dimensional binding constants between cell-bound major histocompatibility complex and immobilized antibodies with an acoustic biosensor. *Biophys. J.* **95**, 4963–4971 (2008).
 33. Dukes, J. D., Whitley, P. & Chalmers, A. D. The MDCK variety pack: choosing the right strain. *BMC Cell Biol.* **12**, 43 (2011).
 34. Maini, P. K., McElwain, D. L. S. & Leavesley, D. Travelling waves in a wound healing assay. *Appl. Math. Lett.* **17**, 575–580 (2004).
 35. Xu, F., Wang, W., Hou, J. & Liu, M. Temperature effects on the propagation characteristics of Love waves along multi-guide layers of SiO₂/Su-8 on St-90°X quartz. *Sensors (Switzerland)* **12**, 7337–7349 (2012).
 36. Kondoh, J., Furukawa, T., Matsui, Y. & Shiokawa, S. Identification of ionic solutions using a liquid flow system with SH-SAW sensors. *Proc. IEEE Ultrason. Symp.* **1**, 389–394 (1996).
 37. Oh, H., Lee, K. J., Baek, J., Yang, S. S. & Lee, K. Development of a high sensitive pH sensor based on shear horizontal surface acoustic wave with ZnO nanoparticles. *Microelectron. Eng.* **111**, 154–159 (2013).
 38. Paschke, B., Wixforth, A., Denysenko, D. & Volkmer, D. Fast Surface Acoustic Wave-Based Sensors to Investigate the Kinetics of Gas Uptake in Ultra-Microporous Frameworks. *ACS Sensors* **2**, 740–747 (2017).

39. Kondoh, J., Saito, K., Shiokawa, S. & Suzuki, H. Simultaneous measurements of liquid properties using multichannel shear horizontal surface acoustic wave microsensor. *Japanese J. Appl. Physics, Part 1 Regul. Pap. Short Notes Rev. Pap.* **35**, 3093–3096 (1996).
40. Janshoff, A., Wegener, J. & Sieber, M. Double-mode impedance analysis of epithelial cell monolayers cultured on shear wave resonators. *Eur. Biophys. J.* **25**, 93–103 (1996).
41. Auld, B. A. *Acoustic Fields and Waves in Solids*. (Krieger Publishing, 1990).
42. Kondoh, J. A liquid-phase sensor using shear horizontal surface acoustic wave devices. *Electron. Commun. Japan* **96**, 41–49 (2013).
43. Li, S. *et al.* Determination of microwave conductivity of electrolyte solutions from Debye-Drude model. *Prog. Electromagn. Res. Symp.* 670–673 (2014).
44. Pethig, R. *Dielectrophoresis: Theory, Methodology and Biological Applications*. (John Wiley & Sons, Ltd, 2017). doi:10.1002/9781118671443
45. Zehnder, S. M., Suaris, M., Bellaire, M. M. & Angelini, T. E. Cell volume fluctuations in MDCK monolayers. *Biophys. J.* **108**, 247–250 (2015).